

Thermodynamic Analysis of Bridging Bubbles and a Quantitative Comparison with the Measured Hydrophobic Attraction

Phil Attard

Ian Wark Research Institute, University of South Australia, Mawson Lakes SA 5095, Australia

Received September 2, 1999. In Final Form: February 9, 2000

The shape of a bubble bridging two colloidal spheres is obtained by minimization of the constrained Gibbs free energy. Bubbles bridging hydrophobic surfaces are concave, whereas hydrophilic surfaces give rise to convex bubbles. Owing to an energy barrier, metastable submicroscopic bubbles are prevented from expanding to microscopic size, and vice versa, and hysteresis is found on approach and on separation of the hydrophobic spheres. The force due to the bridging bubble is generally attractive, except at small separations for both pinned bubbles and hydrophilic surfaces. An analytic approximation for the force and bridging bubble size is derived and shown to be much more accurate for colloidal spheres than the classic formula for the capillary adhesion. Dynamic drag on the expanding bubble is shown to reduce the attraction and to give a repulsion at small separations. The dynamic results give a quantitative account of the force measured between hydrophobic surfaces in water with an atomic force microscope.

Introduction

There have been a number of theoretical mechanisms proposed to account for the long-range attractions measured between macroscopic hydrophobic surfaces in water. These include electrostatic correlations,¹ disturbed water structure,² separation-induced phase transitions,^{3–5} and bridging submicroscopic bubbles.^{6,7} To date most theoretical attention has focused on electrostatic coupling, with anomalous solvent¹ and electrolyte^{8,9} fluctuations and correlated charge domains^{10–12} all being analyzed. However, detailed experimental tests have shown that the force is measurable even at molar electrolyte concentrations,^{6,13–16} which conclusively rules out any electrostatic mechanism in those particular systems.

Of the remaining mechanisms, the proposal by Attard^{6,7} that the force arises from the bridging of submicroscopic bubbles adhering to the surfaces is the most attractive. Originally based upon the observation of steps in the experimental data,⁶ which were interpreted as signifying the bridging of multiple bubbles, the idea has recently

received striking experimental support in the form of atomic force measurements using a hydrophobic colloid sphere, which traps at most a single submicroscopic bubble in the contact region, and which has been argued to yield a clear and unambiguous interpretation.¹⁶ Very similar results have since been obtained by a number of groups,^{17–19} and these, together with other deaeration studies,^{20,21} now provide additional support for the idea that bridging submicroscopic bubbles are responsible for the long-range attractions measured in these systems.

This paper presents a theoretical analysis of a bubble bridging two surfaces, and of the consequent force. The purpose is severalfold. First, the qualitative agreement between the calculated and the measured forces strongly supports the interpretation that the data mentioned above does indeed signify the presence of a bridging bubble. (Because the bridging bubble is submicroscopic and cannot be seen, its presence can only be inferred from the nature of the force curves.) Second, a quantitative fit of the theory to the experimental data provides a way to measure certain physical quantities that cannot be obtained directly. Third, the changes in the calculated forces with various parameters indicate ways to control and exploit the phenomenon. And fourth, beyond the present application to the hydrophobic attraction, the results also apply, at least qualitatively, to a range of similar problems, such as droplet bridging,²² capillary condensation,^{23,24} separation-induced phase transitions in binary mixtures,^{25,26} particles interacting with macroscopic bubbles,^{27,28} and the like. Similarly

- (1) Attard, P. *J. Phys. Chem.* **1989**, *93*, 6441.
- (2) Eriksson, J. C.; Ljunggren, S.; Claesson, P. M. *J. Chem. Soc., Faraday Trans. 2* **1989**, *85*, 163.
- (3) Attard, P.; Ursenbach, C. P.; Patey, G. N. *Phys. Rev. A* **1992**, *45*, 7621.
- (4) Bérard, D. R.; Attard, P.; Patey, G. N. *J. Chem. Phys.* **1993**, *98*, 7236.
- (5) Lum, K.; Chandler, D.; Weeks, J. D. *J. Phys. Chem. B* **1999**, *103*, 4570.
- (6) Parker, J. L.; Claesson, P. M.; Attard, P. *J. Phys. Chem.* **1994**, *98*, 8468.
- (7) Attard, P. *Langmuir* **1996**, *12*, 1693.
- (8) Podgornik, R. *J. Chem. Phys.* **1989**, *91*, 5840.
- (9) Spalla, O.; Belloni, L. *Phys. Rev. Lett.* **1995**, *74*, 2515.
- (10) Tsao, Y. H.; Evans, D. F.; Wennerström, H. *Langmuir* **1993**, *9*, 779.
- (11) Miklavic, S. J.; Chan, D. Y. C.; White, L. R.; Healy, T. W. *J. Phys. Chem.* **1994**, *98*, 9022.
- (12) Miklavic, S. J. *J. Chem. Phys.* **1995**, *103*, 4794.
- (13) Christenson, H. K.; Fang, J.; Ninham, B. W.; Parker, J. L. *J. Phys. Chem.* **1990**, *94*, 8004.
- (14) Christenson, H. K.; Claesson, P. M.; Parker, J. L. *J. Phys. Chem.* **1992**, *96*, 6725.
- (15) Craig, V. S. J.; Ninham, B. W.; Pashley, R. M. *Langmuir* **1998**, *14*, 3326.
- (16) Carambassis, A.; Jonker, L. C.; Attard, P.; Rutland, M. W. *Phys. Rev. Lett.* **1998**, *80*, 5357.

- (17) Considine, R. F.; Hayes, R. A.; Horn, R. G. *Langmuir* **1999**, *15*, 1657.
- (18) Considine, R. F.; Drummond, C. J. *Langmuir* (in press).
- (19) Mahnke, J.; Stearnes, J.; Hayes, R. A.; Fornasiero, D.; Ralston, J. *Phys. Chem. Chem. Phys.* **1999**, *1*, 2793.
- (20) Meagher, L.; Craig, V. S. J. *Langmuir* **1994**, *10*, 2736.
- (21) Wood, J.; Sharma, R. *Langmuir* **1995**, *11*, 4797.
- (22) Mulvaney, P.; Perera, J. M.; Biggs, S.; Grieser, F.; Stevens, G. W. *J. Colloid Interface Sci.* **1996**, *183*, 614.
- (23) Fisher, L. R.; Israelachvili, J. N. *Colloids Surf.* **1981**, *3*, 303.
- (24) Christenson, H. K. *Phys. Rev. Lett.* **1994**, *73*, 1821.
- (25) Boucher, E. A. *J. Chem. Soc., Faraday Trans.* **1990**, *86*, 2263.
- (26) Wennerstrom, H.; Thuresson, K.; Linse, P.; Freysson, E. *Langmuir* **1998**, *14*, 5664.
- (27) Ducker, W. A.; Wu, Z.; Israelachvili, J. N. *Langmuir* **1994**, *10*, 3279.

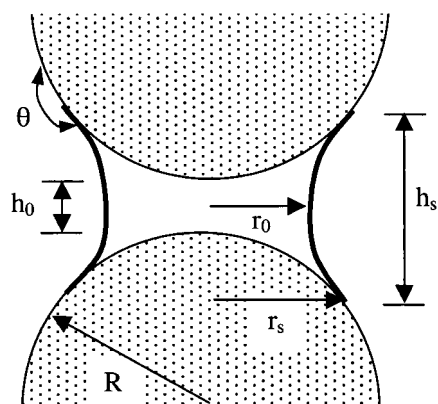


Figure 1. Basic geometry of a bridging bubble between two spheres of radius R and separated by h_0 . The radius of the contact rim is r_s , that of the waist is r_0 , and the contact angle is θ .

the computational algorithm used to obtain the bubble shape may be applied to these and other shape optimization and energy minimization problems.

The paper is divided into two main sections. Section I analyzes the model of the bridging bubble. It presents in turn the thermodynamic analysis, the polynomial expansion of the bubble profile, computational details, an analytic microscopic cylinder approximation, and proof of the contact angle condition for planar surfaces. Section II contains the results and is divided into two parts. The first is the static equilibrium situation, and bubble shape and consequent force are given for a variety of parameters. The second part deals with dynamic effects, specifically the effect of drag on the expanding bubble. It is shown by comparison with measured data that these are necessary to describe the experiments in quantitative detail.

I. Model and Analysis

Figure 1 shows the basic geometry of the bridging bubble. The radius of the two identical spheres is denoted by R , and their separation, which is measured between their surfaces on the axis, is h_0 . The radius of the bridging bubble at its waist is r_0 , and the radius of its rim where it is in contact with the solid is r_s , at which point the surface separation is h_s . The contact angle that the bubble makes with the solid is measured through the liquid phase and is denoted by θ . The exhibited bubble is concave, with $r_0 < r_s$; a convex bubble has $r_0 > r_s$.

The analysis below may readily be extended to two different spheres or to a sphere and a flat. The notation and numerical implementation is somewhat cumbersome for the general problem; since one does not expect any new qualitative features to emerge, only the symmetric case of two identical spheres is pursued here.

It is a matter of simple geometry to show that the surface separation at the bubble rim is given by

$$h_s = h_0 + 2R - 2\sqrt{R^2 - r_s^2} \quad (1)$$

Further, if the slope of the surface of the bubble at the rim is $r'_s \equiv dr(z)/dz|_{z=h_s/2}$, then the contact angle is given by

$$\theta = \pi - \cos^{-1} \frac{r'_s}{R} + \tan^{-1} r'_s \quad (2)$$

Note that these are the full, exact, expressions for the

present spheres. In previous work⁶ only the leading term in r_s/R was retained.

A. Thermodynamics. If the bubble is constrained to have a certain shape, with corresponding volume V_0 , liquid–vapor surface area A_{lv} , and liquid–solid surface area A_s , then the constrained Gibbs free energy is

$$G([r], h_0) = Nk_B T - Nk_B T \ln \Lambda^3 V_0 + p_0 V_0 + \gamma A_{lv} - \Delta\gamma A_s \quad (3)$$

Here N is the number of gas molecules, assumed ideal, k_B is Boltzmann's constant, T is the temperature, Λ is the thermal wavelength, p_0 is the external pressure of the liquid, γ is liquid–vapor surface tension, and $\Delta\gamma = \gamma_{sl} - \gamma_{sv}$ is the difference in solid surface energies. This is related to the equilibrium contact angle at a linear three-phase line between semiinfinite media by the Young equation, $\Delta\gamma = -\gamma \cos \theta_{slv}$. The constrained Gibbs free energy equals $-T$ times the constrained total entropy for a system able to exchange volume with an external reservoir, in thermal equilibrium with it, and with fixed number of molecules. It gives the probability of volume fluctuations, and hence may also be called the fluctuation potential.²⁹ The constrained Gibbs free energy is minimized by the equilibrium volume shape where it equals the equilibrium Gibbs free energy.²⁹ The equilibrium shape may be denoted $\bar{r}(z)$ and the equilibrium energy $\bar{G}(h_0)$, so that one has $G([r], h_0) \geq G(\bar{r}, h_0) = \bar{G}(h_0)$.

Previous studies of capillary forces have mainly focused on open systems,^{6,30–32} where N varies at constant chemical potential, and the grand potential is used. For the present problem of a bridging bubble, it is most appropriate to fix the number of gas molecules (i.e., the bubble is in mechanical and thermal equilibrium, but the gas is not in diffusive equilibrium with the atmosphere).^{6,7} Parker et al.⁶ studied both open systems and the present closed isothermal–isobaric system, but in the latter case they approximated the shape of the bridging bubble as that of a truncated hemisphere. In the present paper the full shape optimization is carried out.

The traditional way of solving problems of this type is to express the volume and areas as a functional of the bubble shape. Setting the functional derivative of the constrained free energy to zero yields an Euler–Lagrange first-order differential equation that may be solved for the equilibrium bubble shape. This was the approach that was pursued in an earlier study of this problem.⁶ The differential equation involves the internal pressure of the bubble, which is fixed and known for an open system, but which must be determined self-consistently from the bubble volume for the present isothermal–isobaric system. This is computationally demanding. A more tractable approach is to parametrize the bubble shape by an appropriate expansion and to minimize the constrained free energy with respect to variation of the coefficients of the expansion. The advantage of this approach is that energy minimization procedures can be very efficient, and the order of the expansion and hence the computational complexity are easily controlled. In general such procedures are robust, which is to say that they are insensitive to small errors in the bubble shape. In addition they allow the exploration of metastable shapes, and of the effects of constrained minimization.

(29) Attard, P. *J. Stat. Phys.*, in press.

(30) Yaminsky, V. V.; Yushenko, V. S.; Amelina, E. A.; Shchukin, E. D. *J. Colloid Interface Sci.* **1983**, *96*, 301.

(31) Yushenko, V. S.; Yaminsky, V. V.; Shchukin, E. D. *J. Colloid Interface Sci.* **1983**, *96*, 307.

(32) Eriksson, J. C.; Ljunggren, S. *Langmuir* **1995**, *11*, 2325.

What now follows is an expansion for the bubble shape and the consequent expressions for the volume and area of the bubble. Also given are explicit expressions for the forces conjugate to the coefficients, since these are used in the minimization procedure.

B. Polynomial Expansion. A cylindrical coordinate system is used, and a position on the bubble surface is parametrized by $x \in [-1, 1]$ such that the axial coordinate is $z(x) = h_s x/2$, and the radial coordinate is $r(x)$. One has $r(0) = r_0$, $r(1) = r_s$, and $r(-x) = r(x)$. In view of these and the symmetry of the problem the bubble surface is expanded as

$$r(x) = r_s + \sum_{n=1}^M a_n (x^{2n} - 1) \quad (4)$$

Throughout r_s and the a_n are the independent variables and the waist radius, $r_0 = r_s - \sum_n a_n$, is a function dependent on them that is not held fixed during partial differentiations. Subject to this caveat, it is convenient to define $a_0 \equiv r_0$; all sums and derivatives involving the a_n are for $n \geq 1$, unless explicitly indicated otherwise. The slope of the surface is $r'(x) \equiv dr(x)/dx = \sum_n 2na_n x^{2n-1}$.

The volume bounded by the bubble in the radial direction and by $-h_s/2 \leq z \leq h_s/2$ in the axial direction is given by

$$\begin{aligned} V &= \frac{\pi h_s}{2} \int_{-1}^1 dx r(x)^2 \\ &= \pi h_s \sum_{n=0}^M \sum_{m=0}^M \frac{a_n a_m}{2n + 2m + 1} \end{aligned} \quad (5)$$

The total volume of the solid spheres included in this is

$$\begin{aligned} V_s &= 4\pi \int_0^{r_s} dr r [\sqrt{R^2 - r^2} - \sqrt{R^2 - r_s^2}] \\ &= \frac{2\pi}{3} [2R^3 - (2R^2 + r_s^2)\sqrt{R^2 - r_s^2}] \end{aligned} \quad (6)$$

The volume of the bubble itself is $V_0 = V - V_s$.

The area of the liquid-vapor interface is

$$A_{lv} = \pi h_s \int_{-1}^1 dx r(x) \sqrt{1 + 4r'(x)^2/h_s^2} \quad (7)$$

The total area of the solid-vapor interface is

$$\begin{aligned} A_s &= 4\pi \int_0^{r_s} dr r \sqrt{1 + \frac{r^2}{R^2 - r^2}} \\ &= 4\pi R [R - \sqrt{R^2 - r_s^2}] \end{aligned} \quad (8)$$

Expressions for the forces conjugate to r_s , and to the a_n , $n > 0$, are now required. That is,

$$F_r \equiv -\frac{\partial G}{\partial r_s} \quad \text{and} \quad F_n \equiv -\frac{\partial G}{\partial a_n}, \quad n > 0 \quad (9)$$

Obviously the evaluation of these forces requires the respective derivatives of the volumes and areas, and these will utilize

$$\frac{\partial r_0}{\partial r_s} = 1, \quad \frac{\partial r_0}{\partial a_n} = -1, \quad n > 0 \quad (10)$$

and

$$\frac{\partial h_s}{\partial r_s} = \frac{2r_s}{\sqrt{R^2 - r_s^2}}, \quad \frac{\partial h_s}{\partial a_n} = 0, \quad n > 0 \quad (11)$$

The derivatives of the bounding volume are

$$\frac{\partial V}{\partial r_s} = \frac{V}{h_s} \frac{\partial h_s}{\partial r_s} + 2\pi h_s \sum_{n=0}^M \frac{a_n}{2n + 1} \quad (12)$$

and

$$\frac{\partial V}{\partial a_n} = 2\pi h_s \sum_{m=0}^M \frac{a_m}{2n + 2m + 1}, \quad n > 0 \quad (13)$$

The derivatives of the volume cut out by the solids are

$$\frac{\partial V_s}{\partial r_s} = \frac{2\pi r_s^3}{\sqrt{R^2 - r_s^2}} \quad (14)$$

and of course $\partial V_s/\partial a_n = 0$, $n > 0$.

The derivatives of the liquid-vapor area are

$$\begin{aligned} \frac{\partial A_{lv}}{\partial r_s} &= \frac{A_{lv}}{h_s} \frac{\partial h_s}{\partial r_s} + 2\pi h_s \int_0^1 dx \left[\sqrt{1 + 4r'(x)^2/h_s^2} - \right. \\ &\quad \left. \frac{4r(x) r'(x)^2/h_s^3}{\sqrt{1 + 4r'(x)^2/h_s^2}} \frac{\partial h_s}{\partial r_s} \right] \end{aligned} \quad (15)$$

and, for $n > 0$

$$\begin{aligned} \frac{\partial A_{lv}}{\partial a_n} &= 2\pi h_s \int_0^1 dx \left[(x^{2n} - 1) \sqrt{1 + 4r'(x)^2/h_s^2} + \right. \\ &\quad \left. \frac{8nx^{2n-1} r(x) r'(x)/h_s^2}{\sqrt{1 + 4r'(x)^2/h_s^2}} \right] \end{aligned} \quad (16)$$

Finally, the derivatives of the solid area are

$$\frac{\partial A_s}{\partial r_s} = \frac{4\pi R r_s}{\sqrt{R^2 - r_s^2}} \quad (17)$$

and $\partial A_s/\partial a_n = 0$, $n > 0$. These expressions, in combination with eqs 3 and 9, give the forces conjugate to r_s and the a_n , $n > 0$.

Finally, the force between the spheres due to the bridging bubble will also be required. This is given by

$$\begin{aligned} F_h &= -\frac{d\bar{G}(h_0)}{dh_0} \\ &= -\frac{\partial G([r], h_0)}{\partial h_0} \Big|_{r(x)=\bar{r}(x)} \\ &= \Delta p \frac{\partial V_0}{\partial h_0} - \gamma \frac{\partial A_{lv}}{\partial h_0} \end{aligned} \quad (18)$$

where the pressure drop is $\Delta p = (NkT/V_0) - p_0$. The second line follows from the variational nature of the fluctuation

potential.²⁹ The requisite derivatives are

$$\frac{\partial V_0}{\partial h_0} = \frac{V}{h_0} \quad (19)$$

and

$$\frac{\partial A_{lv}}{\partial h_0} = \frac{A_{lv}}{h_s} - \frac{8\pi}{h_s^2} \int_0^1 dx \frac{r(x) r'(x)^2}{\sqrt{1 + 4r'(x)^2/h_s^2}} \quad (20)$$

since $\partial h_s/\partial h_0 = 1$ and $\partial V_s/\partial h_0 = 0$.

C. Numerical Details. The number of coefficients used to obtain the results reported below was $M = 20$. Little change was observed upon decreasing this number to five. The integrals for A_{lv} and its derivatives were evaluated numerically using the trapezoid rule. The parameter x was confined to the interior of the unit interval, and the bubble profile $r(x)$ and slope $r'(x)$ were calculated from the expansion and stored on a uniform grid x_i of 500 points. Little change occurred on reducing this to 200 points.

The algorithm for the energy minimization involved calculating the conjugate forces for the current bubble profile and moving the coefficients in the direction of these forces and in proportion to their magnitude, which may be thought of as a conjugate gradient method. The optimization proceeded in two stages: the inner stage was optimization of the profile for fixed r_s , and the outer stage was minimization with respect to r_s . The inner part of the optimization consisted of moving each of the coefficients in the direction of the current (fixed) conjugate forces until the energy no longer decreased, at which stage the forces were recalculated. This procedure was continued until the square root of the sum of the squares of the conjugate forces was less than some residual, typically 10^{-11} N. The energy was minimized with respect to r_s by first finding two values of r_s with opposing forces F_r , thereby bounding the solution, and thence by interval halving. (At each value of r_s the bubble shape was optimized.) The procedure was terminated when either some residual in force was achieved, or some tolerance in r_s , typically 10^{-2} nm. Its worth mentioning that the method of optimization for r_s could have been used successively for each of the a_n in a recursive algorithm.

The validity of the program, the adequacy of the parameters, and the degree of convergence, were checked by comparing the various forces evaluated explicitly as above with numerical differentiation of the free energy. Previous results⁶ were also used to test the present approach.

D. Cylinder Approximation. For hydrophobic surfaces, $\Delta\gamma < 0$, which have obtuse equilibrium contact angles, $\theta_{slv} > \pi/2$, at not too large separations, there is always a stable bridging bubble of microscopic dimensions (see below). In general the volume of a bubble of this shape is much larger than when it is a hemisphere on an isolated surface. Hence the internal gas pressure of the microscopic bridging bubble is much less than the external atmospheric pressure, $Nk_B T/V_0 \ll p_0$. Accordingly, to a good approximation the constrained Gibbs free energy may be written

$$G([r], h_0) \approx p_0 V_0 + \gamma A_{lv} - \Delta\gamma A_s \quad (21)$$

To a very good approximation the microscopic bridging bubble is cylindrical in shape. This may be seen as follows. Consider the saddle-shaped bubble to have internal neck radius r_0 and external radius r_e , and assume that for a microscopic bubble $r_0 \ll r_e$. The total curvature is $r_{tot}^{-1} =$

$r_0^{-1} - r_e^{-1} \approx -r_e^{-1}$, and from the Laplace–Young equation one obtains $r_e \approx -\gamma/\Delta p \approx \gamma/p_0 = 720$ nm, typically. (Alternatively, taking $r_0 \approx 1$ μm yields $r_e \approx 400$ nm.) The difference between the contact radius and the waist radius may be obtained from eq 1, (replacing h_s by r_s , h_0 by r_0 , R by r_e , and r by $h_s/2$, removing the factor of 2, and then expanding to leading order), $r_s - r_0 \approx h_s^2/8r_e$. Similarly the surface separation at the rim to leading order is $h_s \approx h_0 + r_s^2/R \approx r_s^2/R$, so that the relative departure from cylindrical shape is

$$\frac{r_s - r_0}{r_s} \approx \frac{r_s^3}{8r_e R^2} \quad (22)$$

For 10 μm spheres and a 1 μm contact radius, this is about 0.3%.

In view of this, one may well approximate a microscopic bridging bubble as a cylinder of radius r_s (equivalent to setting $M=0$ in the above). In this case the bubble volume is

$$V_0 = \pi r_s^2 h_s - V_s \quad (23)$$

and the liquid–vapor surface area is

$$A_{lv} = 2\pi r_s h_s \quad (24)$$

With this cylinder approximation and the expressions for V_s and A_s given above, the derivative of the approximate constrained Gibbs free energy is

$$\frac{\partial G}{\partial r_s} = p_0 2\pi r_s h_s - \Delta\gamma \frac{4\pi R r_s}{\sqrt{R^2 - r_s^2}} + \gamma \left[2\pi h_s + \frac{4\pi r_s^2}{\sqrt{R^2 - r_s^2}} \right] \quad (25)$$

Setting this to zero gives the equilibrium state. One can solve for the equilibrium contact radius implicitly, $\bar{r}_s(h_0)$. Or one may instead solve explicitly for the equilibrium separation as a function of contact radius

$$\bar{h}_s(r_s) = \frac{2Rr_s\Delta\gamma - 2r_s^2\gamma}{(r_s p_0 + \gamma)\sqrt{R^2 - r_s^2}} \quad (26)$$

This, in combination with eq 1, gives the surface separation for a given contact rim radius, $\bar{h}_0(r_s)$.

The force between the spheres in this approximation is

$$\begin{aligned} F &= \frac{-d\bar{G}(h_0)}{dh_0} \\ &= \frac{-\partial G(r_s, h_0)}{\partial h_0} \Big|_{r_s=\bar{r}_s} \\ &= -\pi r_s^2 p_0 - 2\pi r_s \gamma \end{aligned} \quad (27)$$

This expression is what one would have expected intuitively: the force is attractive and equal to the external pressure times the area of the waist plus the surface tension times the circumference of the waist. This expression gives the force as a function of the contact rim radius. Hence it and the preceding equation are the parametric representation of the force–distance relationship for this bridging microscopic cylinder.

It is useful to give an explicit expression for the maximum attraction or capillary adhesion. With $r_s \ll R$ and $h_0 \ll h_s$, one has $h_s \approx r_s^2/R$, and the above expression reduces to a quadratic equation that may be solved for the contact radius

$$r_s^* \approx \frac{-3\gamma}{2p_0} [1 - \sqrt{1 + 8Rp_0\Delta\gamma/9\gamma^2}] \quad (28)$$

This is the largest radius of the bridging bubble, and insertion in the force equation gives the maximum pull-off force, $F^* = F(r_s^*)$.

For large spheres, $R \rightarrow \infty$, the leading order term gives $r_s^* = (2R\Delta\gamma/p_0)^{1/2}$ and $F^* = -2\pi R\Delta\gamma = 2\pi R\gamma \cos \theta_{slv}$. This is the well-known formula for capillary adhesion.³³ It will be shown below that this classic result is less accurate for colloidal spheres (i.e., $R \lesssim 10 \mu\text{m}$), than the microscopic cylinder approximation.

It should be pointed out that there is nothing specific to a bridging bubble assumed in the derivation of the results in this section. For the case of capillary condensation, for example, simply replace p_0 by $-\Delta p = -(k_B T\rho_l) \ln[p_v/p_{v0}]$, (ρ_l is the liquid number density, and the argument of the logarithm is the relative vapor pressure), and set $\Delta\gamma = \gamma \cos \theta_{slv} > 0$.

E. Contact Angle Condition. When one has three semiinfinite media mutually bounded by planar interfaces such that the contact line is straight, then it is straightforward to derive the Young–Laplace equation from simple force balance considerations

$$\Delta\gamma = -\gamma \cos \theta_{slv} \quad (29)$$

The reason that the derivation of this is trivial is that there is no pressure drop across the flat interfaces (hence no $p \, dV$ work), and the change in interfacial area is linear in the displacement of the contact line.

For the case of a bubble in contact with a solid surface, these simplifying conditions no longer hold, but one may nevertheless show using only elementary algebra that the bubble radius and contact angle that minimize the constrained Gibbs free energy are precisely those that satisfy the Laplace and the Young–Laplace equations, respectively.^{6,7}

In the case of a bubble bridging two spheres, the algebra proliferates and the analysis is complicated by the geometry. Here the simpler case of a bubble bridging two planar surfaces is analyzed. In this case the surface separation is $h_s = h_0 = h$, $V_s = 0$, and $A_s = 2\pi r_s^2$. One has

$$\frac{\delta V_0}{\delta r(x)} = \pi h r(x) \quad (30)$$

$$\frac{\delta A_{lv}}{\delta r(x)} = \pi h \sqrt{1 + 4r'(x)^2/h^2} - \frac{4\pi}{h} \frac{d}{dx} \frac{r(x) r'(x)}{\sqrt{1 + 4r'(x)^2/h^2}} + \frac{4\pi}{h} \frac{r(x) r'(x)}{\sqrt{1 + 4r'(x)^2/h^2}} [\delta(1+x) + \delta(1-x)] \quad (31)$$

and

$$\frac{\delta A_s}{\delta r(x)} = 2\pi r(x) [\delta(1+x) + \delta(1-x)] \quad (32)$$

The functional derivative of the constrained Gibbs free

energy is

$$\frac{\delta G([r], h)}{\delta r(x)} = -\Delta p \frac{\delta V_0}{\delta r(x)} + \gamma \frac{\delta A_{lv}}{\delta r(x)} - \Delta\gamma \frac{\delta A_s}{\delta r(x)} \quad (33)$$

Setting this to zero on the interior of the interval yields the well-known Euler–Lagrange equation for the liquid–vapor interface, which is equivalent to the Laplace equation

$$0 = -\Delta p \pi h r(x) + \gamma \left[\pi h \sqrt{1 + 4r'(x)^2/h^2} - \frac{4\pi}{h} \frac{d}{dx} \frac{r(x) r'(x)}{\sqrt{1 + 4r'(x)^2/h^2}} \right] \quad (34)$$

Setting the coefficient of the δ -functions to zero yields, with $r'_s \equiv (h/2) \, dr(x)/dx|_{x=1}$

$$0 = \gamma \frac{2\pi r_s r'_s}{\sqrt{1 + (r'_s)^2}} - \Delta\gamma 2\pi r_s \quad (35)$$

or

$$\frac{\Delta\gamma}{\gamma} = \frac{r'_s}{\sqrt{1 + (r'_s)^2}} \equiv -\cos \theta \quad (36)$$

where the right-hand side follows from simple geometry. Hence this shows that the equilibrium contact angle of a bubble bridging two planar surfaces also satisfies the Young–Laplace equation, $\theta = \theta_{slv}$. Numerical results presented below indicate that this conclusion also holds for a bubble bridging two spheres.

II. Results

A. Theory. Figure 2 shows the (semiconstrained) Gibbs potential for a bridging bubble, as a function of the contact radius but otherwise optimized with respect to shape, for several separations of the hydrophobic spheres. It may be seen in Figure 2A that for separations $h_0 \leq 70 \text{ nm}$ there is a stable microscopic bridging bubble, and that the radius increases with decreasing separation. At larger separations, $h_0 = 80$ and 90 nm , the microscopic bridging bubble is metastable with respect to the submicroscopic one (see Figure 2B) and beyond $h_0 = 90 \text{ nm}$ the microscopic bubble is unstable. In other words, Figure 2B shows that at large separations (in this case $h_0 = 80$ and 90 nm) the stable bridging bubble is of submicroscopic size, and that for separations $h_0 = 60$ and 70 nm the submicroscopic bubble is metastable with respect to the microscopic one. The submicroscopic bubble is unstable for $h_0 \leq 51 \text{ nm}$. Beyond $h_0 = 111 \text{ nm}$ no bubble can stably bridge the surfaces with these parameters.

In view of the results in Figure 2 for the Gibbs potential as a function of the contact radius, one anticipates that there will be hysteresis in the behavior of the bridging bubble on approach and separation of the spheres. On approach, following attachment at large separations, the bridging bubble is initially of submicroscopic size. It remains trapped in this metastable state as the separation is decreased until $h_0 = 51 \text{ nm}$, whereupon it grows to microscopic size. Upon separation the spheres from contact, the bubble is initially microscopic and remains trapped in this metastable state until $h_0 = 90 \text{ nm}$, when it shrinks to submicroscopic size. The bridging bubble snaps at $h_0 = 111 \text{ nm}$.

(33) Hunter, R. J. *Foundations of Colloid Science*; Oxford University Press: Oxford, 1986; Vol. I; Chapter 5.

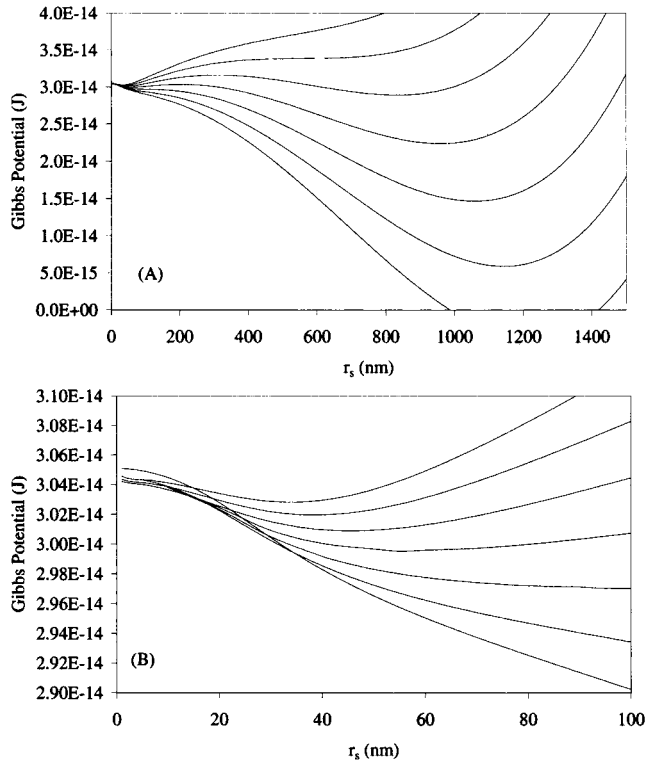


Figure 2. (A) Constrained Gibbs potential as a function of the contact rim radius r_s of a bubble of otherwise optimal shape bridging two spheres (of radius $R = 20 \mu\text{m}$) at surface separations of, from bottom to top, $h_0 = 30, 40, 50, 60, 70, 80,$ and 90 nm . The liquid–vapor surface tension is $\gamma = 0.072 \text{ N m}^{-1}$, and the external pressure is $p_0 = 10^5 \text{ N m}^{-2}$. The contact angle is $\theta = 100^\circ$, and the fixed number of gas molecules in the bubble is $N = 1.4 \times 10^5$, which corresponds for an isolated surface to a hemispherical bubble of radius $R_b = 50 \text{ nm}$ protruding $z_b = 41.32 \text{ nm}$ above the surface. (B) An expanded view for small r_s .

The calculations reveal that the contact angle the bridging bubble makes with the spheres equals the bulk contact angle for all stable and metastable configurations, $\theta = \theta_{\text{slv}}$ (not shown). As shown above, it is straightforward to prove that this should be the case for a bubble bridging planar surfaces. However, geometrical factors make an explicit proof complicated for curved surfaces.

Figure 3 shows the optimal shape of the bridging bubble of Figure 2 as a function of separation. It can be seen that although the microscopic bubbles of Figure 3A are definitely concave, $r_0 < r_s$, on the scale of figure the curvature in the profile is relatively negligible. For example, at $h_0 = 0 \text{ nm}$, one has $r_s = 1356.4 \text{ nm}$ and $r_0 = 1353.6 \text{ nm}$; at $h_0 = 50 \text{ nm}$, one has $r_s = 1057.8 \text{ nm}$ and $r_0 = 1054.5 \text{ nm}$; and at $h_0 = 70 \text{ nm}$, one has $r_s = 832.2 \text{ nm}$ and $r_0 = 828.8 \text{ nm}$. This suggests that the macroscopic cylinder approximation of section I.D will prove accurate. Indeed for the three contact radii just mentioned, that approximation predicts separations of $\bar{h}_0(r_s) = -2.3, 47.6,$ and 67.4 nm , respectively, which are quite close to the actual separations.

Another noticeable feature of Figure 3A is that the surface separation at the rim, h_s , which is the height of the cylindrical bubble, is almost constant and independent of h_0 . From the macroscopic cylinder approximation, it is straightforward to show that $d\bar{h}_s/dr_s \approx (R\bar{h}_0 - r_s^2)/Rr_s$, which, for the parameters of Figure 3, vanishes when $h_0 = r_s^2/R = \mathcal{A}(50 \text{ nm})$, and which is $\mathcal{O}(10^{-2})$ for a 10 nm change in h_0 .

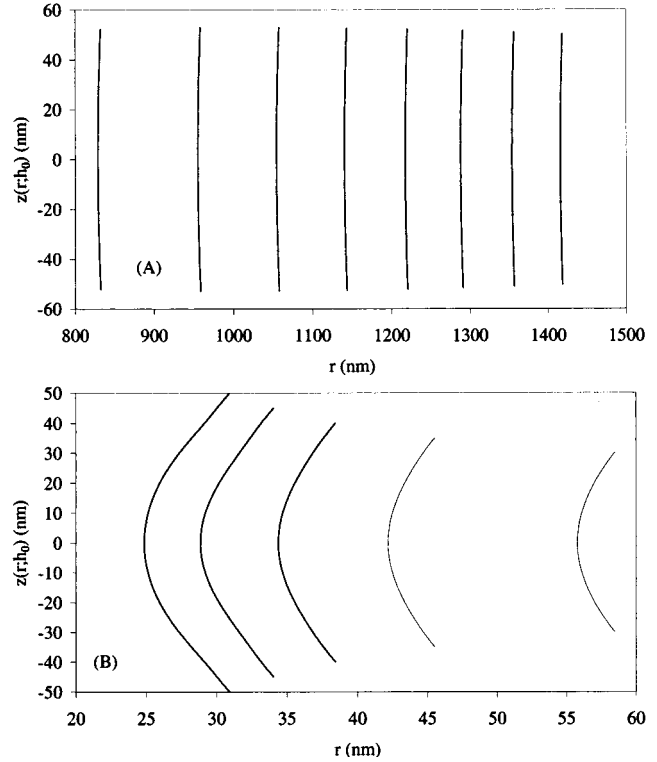


Figure 3. Shape of the unconstrained bridging bubble (parameters as in Figure 2) at various separations. (A) Large microscopic bubbles at separations of, from right to left, $h_0 = 0, 10, 20, 30, 40, 50, 60,$ and 70 nm . (B) Bubbles of submicroscopic radius at separations of, from right to left, $h_0 = 60, 70, 80, 90,$ and 100 nm . The first two are metastable with respect to their microscopic counterparts.

It is clear from Figure 3B that the submicroscopic bridging bubbles are qualitatively different from the microscopic bubbles. They are relatively much more concave in shape, and their height at contact h_s is much more dependent upon the separation h_0 . As the separation is decreased, the submicroscopic bubble grows in radius and becomes less concave.

Figure 4 shows the attractive force between the surfaces that arises from an optimum bubble bridging them. In general the magnitude of the force monotonically increases with decreasing separation. At large separations, the bubble is submicroscopic and the force is weak. At small separations, the bubble is microscopic and there is a strong attraction between the surfaces. There is hysteresis between the approach and separation curves in the region $52 \leq h_0 \leq 79 \text{ nm}$ as the bubble remains trapped in metastable states. The sudden jumps in force between the two runs correspond to the transitions between a submicroscopic and microscopic bubble. These transitions represented a numerical challenge, and up to several thousand iterations were required for convergence at these points.

Also shown in Figure 4 is the microscopic cylinder approximation. It is parabolic in shape and consists of two branches: on the nonphysical branch the attraction decreases with decreasing separation. It may be seen that the physical branch is in good agreement with the numerical results along almost the whole microscopic curve, even predicting the transition to a submicroscopic bubble with relative accuracy. This confirms the efficacy of the approximation: the shape of microscopic bridging bubbles may be accurately modeled as cylindrical, and one may neglect their internal pressure with little error.

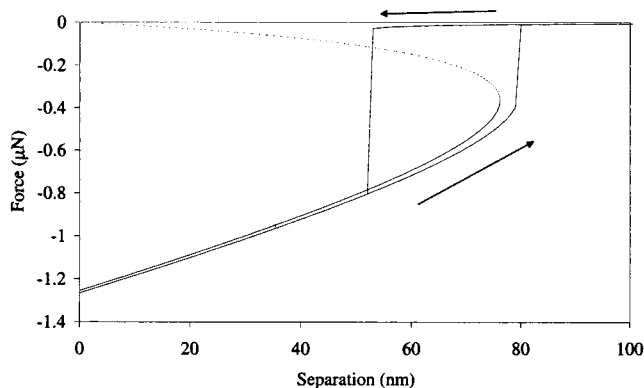


Figure 4. Force between two spheres ($R = 20 \mu\text{m}$), due to an unconstrained bridging bubble (parameters as in Figure 2). At large separations the bubble is submicroscopic (and the attraction is consequently weak), which persists on approach of the surfaces until $h_0 = 50 \text{ nm}$ where it grows to microscopic size, as manifest by jump in the magnitude of the attraction. Upon separation the bubble remains microscopic until $h_0 = 80 \text{ nm}$, where it jumps to the submicroscopic branch. Also shown is the analytic microscopic cylinder approximation, which is parabolic in shape and which is shown dotted on the unstable branch.

The maximum attraction that occurs in Figure 4 is $1.27 \mu\text{N}$, for which the rim radius is $r_s = 1.418 \mu\text{m}$. A classic result for the capillary adhesion of two spheres gives for the external radius³³

$$r_e = -r_s^2/2R \cos \theta \quad (37)$$

which assumes that the spheres are in contact, $h_0 \approx 0$, that they are large compared to the bubble, $R \gg r_s$, and that the bridging bubble is an inverse spheroid of revolution. One then invokes the Laplace equation for the radius $\Delta p = \gamma(r_s^{-1} - r_e^{-1}) \approx -\gamma/r_e$, to give the force of adhesion³³

$$F \approx \Delta p \pi r_s^2 \approx 2\pi\gamma R \cos \theta \quad (38)$$

(As mentioned above, this may also be derived as the $R \rightarrow \infty$ limit of the explicit cylinder approximation, eq 28.) For the case of Figure 4, this classic approximation gives a radius of $r_s = 2.2 \mu\text{m}$ and an adhesion of $1.57 \mu\text{N}$, which are both significantly larger than the exact result. Obviously adding the surface tension to the Laplace contribution will make the adhesion even larger. It may be mentioned in passing that there is experimental evidence that the classic theory overestimates the adhesion.²³ The explicit form of the cylinder approximation, eq 28, gives as the rim radius $r_s^* = 1.403 \mu\text{m}$, and the adhesion as $F^* = -1.25 \mu\text{N}$, which are very close to the actual results. (These explicit results differ by less than 0.1% from the full implicit cylinder approximation.) It may be concluded that the cylinder approximation for the adhesion, whether explicit or implicit, significantly improves upon the traditional result based upon the Laplace pressure drop and using a spherical approximation for the complement of the bubble shape. The reason for the better performance of the cylinder approximation is that it is based upon energy minimization, and such variational procedures are known to be robust and insensitive to approximations.

Note that the force calculations in Figure 4 do not take into account the height of the bubble before it bridges. In particular the transition from submicroscopic to microscopic radius on approach is not related to the height of

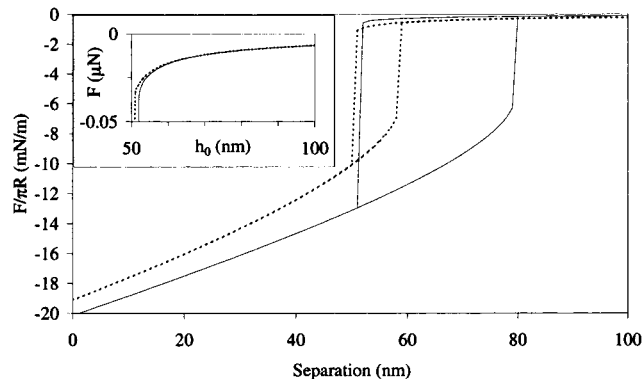


Figure 5. Force due to an unconstrained bridging bubble between identical spheres of radius $R = 20$ and $10 \mu\text{m}$ (full and dotted curves respectively) (all other parameters as in Figure 2). In the main figure the force is normalized by the sphere radius, and in the inset, which shows the submicroscopic branch, the actual force is plotted.

the bubble prior to bridging. On an isolated surface the bubble sits as a hemisphere whose radius and height are determined by the contact angle and the number of confined gas molecules.⁶ In the case of Figures 2–4, the hemispherical bubble has radius $R_b = 50 \text{ nm}$, contact radius $r_b = 49.2 \text{ nm}$, and height above the surface $z_b = 41 \text{ nm}$. The calculated force in Figure 4 is for a bridging bubble at a given separation irrespective of whether this is greater than or less than z_b ; this may be regarded as the envelope of possible forces, and in no way does it prejudice the issue of precisely where the attachment occurs. In the absence of surface forces between the bubble and the sphere, one could argue that attachment occurs when the separation equals the height of the bubble on the isolated surface, and that on approach prior to this the force is zero. This issue will be addressed in detail in the next section when comparison is made with experimental data. In the meantime similar comments hold for all the force curves presented in this section.

Figure 5 shows the force due to a given bubble depends on the size of the spheres. To leading order the force is proportional to the sphere radius, as indicated by the relatively small difference in the two curves in the main figure. (It is the force divided by radius that is plotted here, as dictated by the Derjaguin approximation.) The classic approximation discussed above and the large R limit of the cylinder approximation both predict such a scaling with size. The fact that the scaled attraction for the $10 \mu\text{m}$ sphere is still less than that for the $20 \mu\text{m}$ sphere indicates that the dependence upon radius is stronger than linear. The significance of this plot is that the Derjaguin approximation, although qualitatively correct, is not an exact result for the present bridging bubble. Thus the present capillary force represents one of the few, possibly the only, surface force known to violate the Derjaguin approximation. Despite the fact that quantitatively the Derjaguin approximation has limited accuracy, qualitatively it remains a useful approach. The primary reason that it fails is that the curvature of the surfaces is a strong determinant of the bubble radius as it sets the contact angle. On the submicroscopic branch (see the inset), the actual force between the spheres is almost independent of the radius, owing to the fact that surface of the different spheres is almost flat in equal measure close to the axis. Again this shows that the Derjaguin approximation is indeed an approximation for this problem.

Figure 6 compares the force upon approach for different sized bubbles. The transition from the submicroscopic to

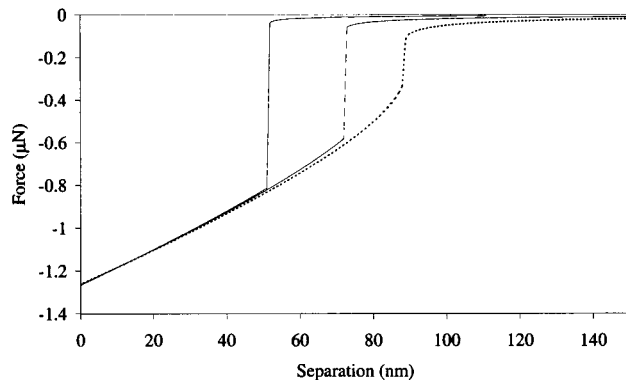


Figure 6. Effect of bubble size upon the approach force (all other parameters as in Figure 2). From left to right the fixed number of gas molecules in the bubble is given by $N = 1.4 \times 10^5$, 3.3×10^5 , and 5.88×10^5 . These correspond to a hemispherical bubble on an isolated surface of radius $R_b = 50$, 75, and 100 nm, and heights above the surface of $z_b = 41.3$, 62.0, and 82.6 nm, respectively.

the microscopic branch occurs within 1 nm of reaching $h_0 = 52$, 73, and 89 nm, in order of increasing bubble size. Although the number of gas molecules N in the bubbles varies by a factor of 4, the forces on the microscopic branch are almost coincident. (The forces upon separation, which are not shown, would also be almost coincident, and on a greater domain.) This is consistent with the conclusion from Figure 4 regarding the validity of the microscopic cylinder approximation. The fact that this approximation is independent of N explains why there is little variation in the force for the three bubbles shown here. On the submicroscopic branch the attraction increases with increasing bubble size.

The semiconstrained Gibbs free energy for a bubble bridging hydrophilic surfaces ($\theta_{slv} = 80^\circ$) is shown in Figure 7A for various surface separations. (Here hydrophilic is used in a mathematical sense to denote surfaces with contact angles less than 90° ; many people would argue on physical grounds that the present surfaces should still be considered hydrophobic.) In this case there is no microscopic bridging bubble, and the energy minima shown at submicroscopic radii are global minima. The reason for this is that the bulk contact angle is acute, and the only way to achieve this is for the bubble to be convex. But microscopic bubbles have low internal pressure, and hence their optimum shape would be concave, and so there cannot be an energy minimum for large radii as there is for hydrophobic surfaces. As the separation is decreased the optimum radius grows but remains submicroscopic. At very small separations the bubble becomes increasingly convex (as the internal gas pressure increases owing to the shrinking volume), and it is again impossible to satisfy simultaneously the bulk contact angle condition. Hence the depth of the energy minimum increases with decreasing separation down to $h_0 = 30$ nm, and then it starts to decrease.

Figure 7B shows the bubble shape for the same separations as in part A. It can be seen that for these hydrophilic surfaces the bubble is convex, in contrast to the bubbles between hydrophobic surfaces of Figure 3, and that the convexity increases as the separation decreases. As for the hydrophobic surfaces, the equilibrium contact angle of the bridging bubble equals the bulk contact angle. The increasing convexity of the bubble indicates that the internal gas pressure is also increasing, and consequently one can expect the force due to the bridging bubble to be repulsive at small separations.

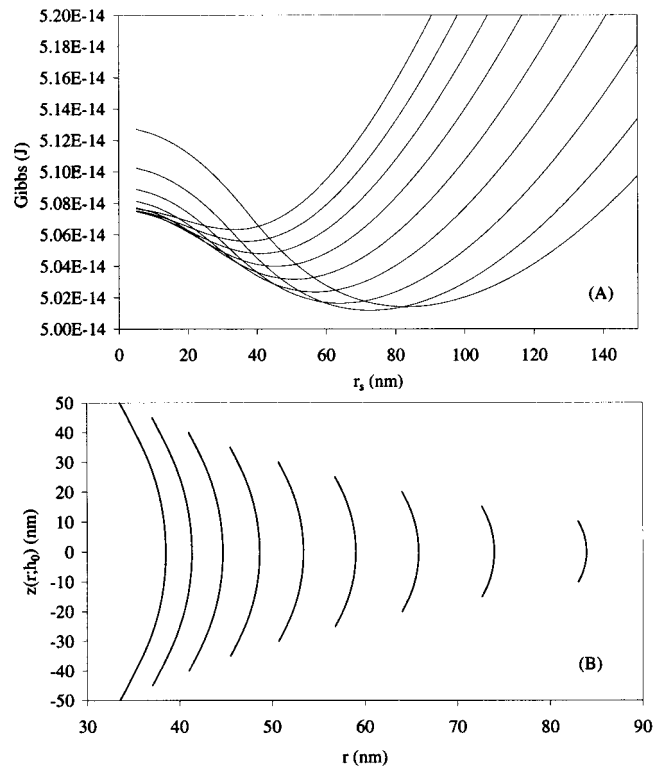


Figure 7. (A) Gibbs potential of a bubble constrained by the contact rim radius but otherwise of optimal shape. The bulk contact angle is $\theta = 80^\circ$, and the separations are, from bottom to top at large radii, $h_0 = 20, 30, 40, 50, 60, 70, 80, 90,$ and 100 nm. All other parameters are as in Figure 2 (except that the number of confined gas molecules is $N = 2.4 \times 10^5$, which corresponds to $R_b = 50$ nm and $z_b = 58.7$ nm). (B) From right to left, for the respective separations, the unconstrained bubble shapes.

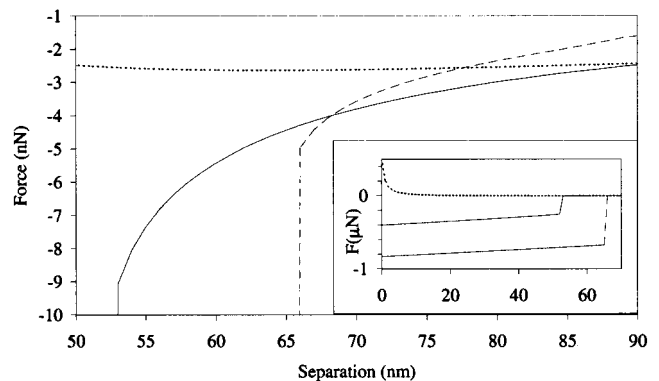


Figure 8. Force between spheres due to a bridging bubble for surfaces with contact angles of $\theta = 100^\circ$ (solid curve), 110° (dashed curve), and 80° (dotted curve). All other parameters are as in Figure 2, except of course the number of molecules and the height of the bubble on an isolated surface.

Figure 8 looks at the effect of the surface energy on the force due to the bridging bubble. As the hydrophobicity of the surface is increased (i.e., $\Delta\gamma$ is made more positive), the transition to the microscopic branch on approach occurs at larger separations. Interestingly enough, on the submicroscopic branch the attraction *decreases* as the hydrophobicity is increased. This is due to the increased difficulty of realizing $\theta = \theta_{slv}$ for large values of θ . Also shown is the bubble bridging the hydrophilic surfaces described in the preceding figure. At large separations the force is attractive, which is perhaps surprising, but which can be rationalized by the recognition that it is

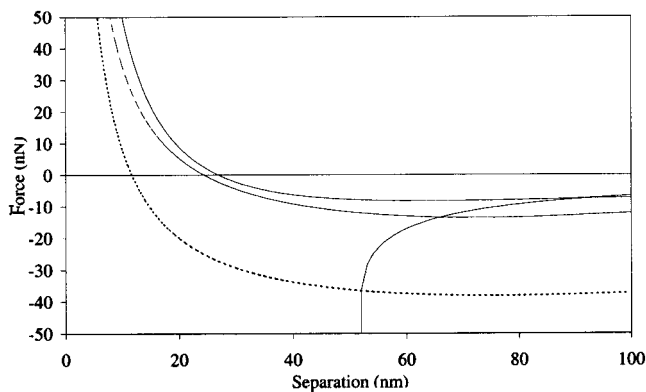


Figure 9. Force between spheres due to a bridging bubble (all parameters as in Figures 2 and 7). The solid curves are for the unconstrained bubble (the cases of $\theta = 100^\circ$ and $\theta = 80^\circ$ are shown), and the dashed and the dotted curves are for a bubble with contact radius pinned at $r_s = 50$ and 100 nm, respectively.

favorable even for hydrophilic surfaces to replace liquid–vapor and liquid–solid contact by vapor–solid contact, and that the area of such contact increases with decreasing separation as the bulk contact angle is maintained. At small separations the force between hydrophilic surfaces becomes strongly repulsive (c.f. the discussion of the energy minima in the preceding figure). This is in contrast to the behavior of the bubble bridging the hydrophobic surfaces, where at small separations the bubble grows to microscopic size and the force is large and attractive, where attraction clearly increases with increasing hydrophobicity.

Finally, Figure 9 explores the effect of pinning the contact radius. The force in this case is still given by eq 18 because $r_s = \text{const}$. Obviously the solid surface energies are irrelevant for such a pinned bubble, and the fact that these are hydrophobic surfaces is immaterial. In this case the force is very different from that of a free bubble between hydrophobic surfaces and qualitatively resembles that of a free bubble between hydrophilic surfaces, which is also shown. For the pinned bubble the force is weakly attractive and almost constant at large separations, and becomes repulsive at small separations. The latter behavior can again be understood in terms of an increasingly convex bubble of small volume, with the repulsion in large part arising from the increase in the internal pressure. The larger the pinned contact radius, the stronger the large separation attraction and the weaker the small separation repulsion.

B. Dynamic Repulsion. To this point only the static situation has been explored, with the bubble either in a stable or metastable equilibrium state, or else with the contact radius pinned. It has recently been shown that dynamic effects can be important in modern surface force measurement,^{34,35} and now the analysis is extended to include motion of the surfaces and of the contact line.

In the case of the atomic force microscope (AFM), which is analyzed in detail below, the resonance frequency of the cantilever is of the order of $10\text{--}40$ kHz,^{35,36} whereas the sampling frequency for data acquisition is of the order of 2 kHz. Hence for practical purposes one may analyze the data as if it were a static force measurement, which is to say that the surface force at any instant is given by the deflection of the cantilever spring times the spring constant, $F_h = kd$.

In view of this, for the AFM the main effects of dynamics are those due to the motion of the spreading bubble. Here the quasi-steady-state situation is analyzed. A drag force is invoked that opposes the expansion in proportion to the velocity of the contact area

$$F_d = -br_s \dot{r}_s \quad (39)$$

Here b is the drag coefficient, which is taken as constant. Such drag could, for example, arise from the hydrodynamic flow of the water between the spheres due to the expanding bubble. In this case the drag force is roughly proportional to the rate of change of volume of the bubble and inversely proportional to the surface separation (cf. Taylor's expression for the drainage force between spheres in Reynolds lubrication approximation³⁷), which gives the above functional form. Localized temporary pinning of the contact rim (e.g., by asperities) would also give rise to this type of drag. It is also worth mentioning that the well-known phenomenon of contact angle hysteresis between advancing and receding contact lines, and its velocity dependence, implies the existence of contact line drag. One could of course generalize the study to include drag opposing the volume expansion of the bubble, but only the simplest model is treated here.

In the steady state the drag force has to be balanced by the thermodynamic force

$$\frac{\partial G}{\partial r_s} + br_s \dot{r}_s = 0 \quad (40)$$

In the limit $b \rightarrow 0$, this is just the stable or metastable equilibrium situation dealt with above. Conversely the limit $b \rightarrow \infty$ corresponds to the case of a pinned bubble, $\dot{r}_s = 0$. Finite values of the drag coefficient mean that the bubble expands with finite velocity, never quite achieving the equilibrium state.

What is also required is the surface force due to the bridging bubble. For this eq 18 is used. This equation holds both for the free and for the pinned bubble, and so it may also be used for intermediate values of b . Using this expression is valid for the steady state, and so it is implicitly assumed that the acceleration of the contact rim is negligible, which is likely a good approximation everywhere except immediately following attachment.

It is numerically straightforward to solve the equations of motion using simple time-stepping. For the current separation h_0 , bubble shape a_n , and contact radius r_s , the thermodynamic force F_r is known and used in eq 40 to give the spreading velocity \dot{r}_s . Upon incrementing time, $t \Rightarrow t + \Delta t$, the radius becomes $r_s \Rightarrow r_s + \Delta t \dot{r}_s$, and the lower surface is moved to $z \Rightarrow z + \Delta t \dot{z}$, where \dot{z} is the fixed drive velocity. Fixing r_s and z , one finds self-consistently the separation, $h_0 = d - z$, and the cantilever deflection, $d = F_r(h_0, r_s)/k$. This is done using the "outer" algorithm described in section I.C., with r_s replaced by h_0 , and optimizing the bubble shape for each trial separation. Finally, the new radial velocity is calculated from the current radial force F_r before incrementing time once more. Typically the time step used to solve the equations is $0.1\text{--}0.01$ of the sampling period used for plotting.

The initial conditions are problematic. In general the initial separation was chosen to equal the height of the bubble on the isolated surface, $h_0(0) \approx z_n$. That is, there are no preattachment forces, and bubble attachment

(34) Attard, P.; Schulz, J.; Rutland, M. W. *Rev. Sci. Instrum.* **1998**, *69*, 3852.

(35) Attard, P.; Carambassis, A.; Rutland, M. W. *Langmuir* **1999**, *15*, 553.

(36) Sader, J. E. *Rev. Sci. Instrum.* **1998**, *69*, 64.

(37) Taylor, G. I. acknowledged by the following: Hardy, W.; Bir-cumshaw, I. *Proc. R. Soc. London A* **1925**, *108*, 1. Derjaguin, B. V.; Krotova, N. A. *Adhesion*, USSR Academy of Science: Moscow, 1949.

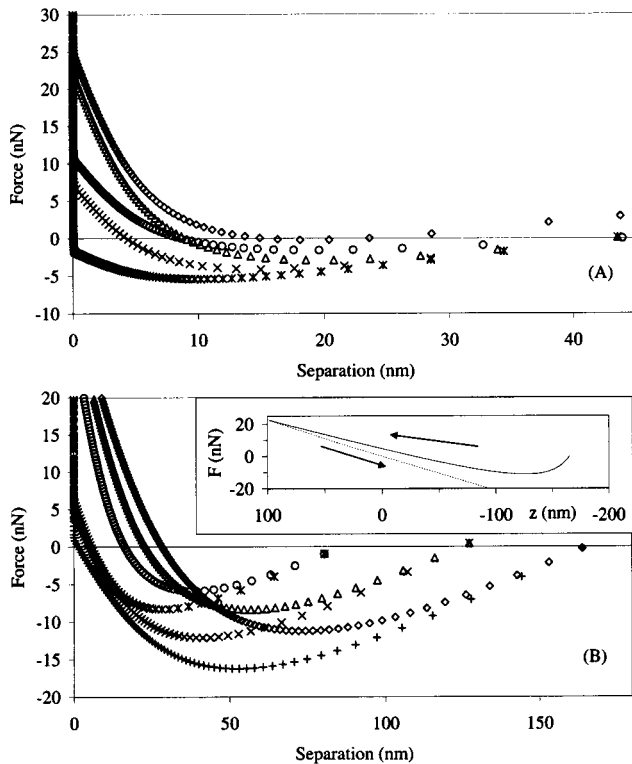


Figure 10. Force due to an expanding bridging bubble (sampling period is 0.5 ms, all unspecified parameters as in Figure 2). In (A), the bubble size is $R_b = 50$ nm, and attachment is taken to begin at the separation corresponding to the height of the bubble on a single surface ($h_0 \approx z_b = 41$ nm). The canonical case (triangles) has initial contact radius $r_{s0} = 25$ nm, drag coefficient $b = 20$ kN s m^{-2} , driving velocity $\dot{z} = 4.5$ $\mu\text{m s}^{-1}$, and spring constant $k = 0.213$ N m^{-1} . The remaining cases also have these values, except that the diamonds correspond to $r_{s0} = 1$ nm, the crosses correspond to $b = 10$ kN s m^{-2} , the asterisks correspond to $\dot{z} = 1$ $\mu\text{m s}^{-1}$, and the circles correspond to $k = 0.1$ N m^{-1} . In (B) everything is as in the canonical case except that the bubble sizes for the three pairs of curves are, from left to right, $R_b = 100$ nm, ($z_b = 83$ nm and $r_{s0} = 60$ nm), $R_b = 150$ nm ($z_b = 124$ nm and $r_{s0} = 80$ nm), and $R_b = 200$ nm, ($z_b = 165$ nm and $r_{s0} = 115$ nm). The open symbols correspond to $b = 20$ kN s m^{-2} , and the characters correspond to $b = 10$ kN s m^{-2} . The inset shows the force as a function of driving position on approach (full) and on separation (dotted) for the 200 nm bubble with the larger drag coefficient.

occurred when the height of the bubble located on one sphere first equaled the surface separation of the spheres. In most cases the initial radius r_{s0} was set so that there was initially no force, $F_b(h_0(0), r_{s0}) \approx 0$. Only the symmetric spreading bubble is treated here, $r(z; t) = r(-z; t)$; in reality, immediately following attachment the bubble must be asymmetric. (On the attaching surface the radius of the bubble grows from zero, and on the other surface it initially shrinks from its original value. After some time the two radii reach the same value, at which point both grow and the present symmetric calculations are most applicable.) Hence because of this, and the neglect of preattachment forces and the neglect of inertial terms mentioned above, in comparing with experiment the initial part of the force curve must be regarded as less quantitative than the remainder.

Figure 10 illustrates the effects of drag on the spreading bubble. The parameters are chosen to mimic a typical AFM experiment, with \dot{z} being the velocity with which the lower sphere is driven toward the upper sphere, which is mounted on the cantilever spring. Compared to the static equilibrium result in Figure 4, the attraction is greatly

reduced (by more than a factor of 100). The attraction is even smaller than that due to pinned bubbles for the particular radii of Figure 9. For the canonical case, by the time the spheres have come into contact in Figure 10A, the bubble has only grown to $r_s = 350$ nm (average velocity $\dot{r}_s = 9.4$ $\mu\text{m s}^{-1}$), which may be compared with the equilibrium value of $r_s = 1.4$ μm for Figure 4. By the time the largest load shown in the figure is applied, the canonical bubble has only grown to $r_s = 407$ nm, and the instantaneous velocity is down to $\dot{r}_s = 70$ $\mu\text{m s}^{-1}$. This radius is larger than that of the pinned bubbles in Figure 9, and consequently the precontact repulsion is softer for this spreading bubble than for those pinned bubbles. Compared to a free bubble, in which the attraction is monotonically increasing, the effect of nonzero drag is to place an upper bound on the attraction. Compared to a pinned bubble, the expanding bubble has lower maximum attraction and softer precontact repulsion.

Obviously the attraction due to the expanding bridging bubble is decreased by increasing the drag, decreasing the initial radius of the bubble, or driving the surfaces together at a faster velocity (Figure 10A). For small enough r_{s0} the initial force can be made repulsive, and effectively the whole force curve is shifted up. This case is a little unrealistic because of the enforced symmetry in the present calculations. Contrarily, a larger initial radius gives an initial attraction and makes the whole force curve more attractive.

The large spacing between the sampled points following initial attachment indicates that the spheres are moving with high velocity toward each other owing to the sudden onset of the attractive force. Although the velocity then slows, the attraction initially continues to increase as the surfaces are brought toward contact, owing to the bubble continuing to spread. This is in contrast to pinned bubbles and to surfaces with bulk contact angle less than 90° ; in Figure 9 it was shown that in these cases the attraction remains relatively constant over an extended range and that there is no increase in the magnitude of the attraction. As the separation is further decreased, the force becomes less attractive before finally turning into a repulsion as shown in Figure 10. This is very similar to the pinned bubble case and has the same physical origin: the bubble is more convex and the volume is smaller than is optimal. In the present case the contact radius continues to grow and eventually the surfaces come into intimate contact, $h_0 \approx 0$. In Figure 10 a short-ranged sphere–sphere repulsion has been included between the surfaces, ($f\sigma^3/h_0^3$, with $f = 10$ nN and $\sigma = 0.1$ nm), which is manifest by the region where the data appears coincident with the ordinate. The more slowly the bubble spreads, the more delayed is the transition to intimate contact, so that, depending upon the maximum load applied, the surfaces themselves may never come into contact. In this event one may mistake the relatively soft repulsion due to the squashing of the bubble with a region of constant compliance, since the repulsion is approximately linear over a limited range.

Figure 10B shows the dependence of the force due to a spreading bubble upon bubble size. In general the range of the force, the magnitude of the maximum attraction, and the softness of the precontact repulsion all increase with bubble size. In the case of the lower drag coefficient, for these bubble sizes the surfaces have not yet come into contact at the maximum force shown.

The inset of Figure 10B shows the force as a function of the position of the driving surface, which is how the raw experimental data is obtained. The surfaces are driven together (approach), and then the direction of motion is

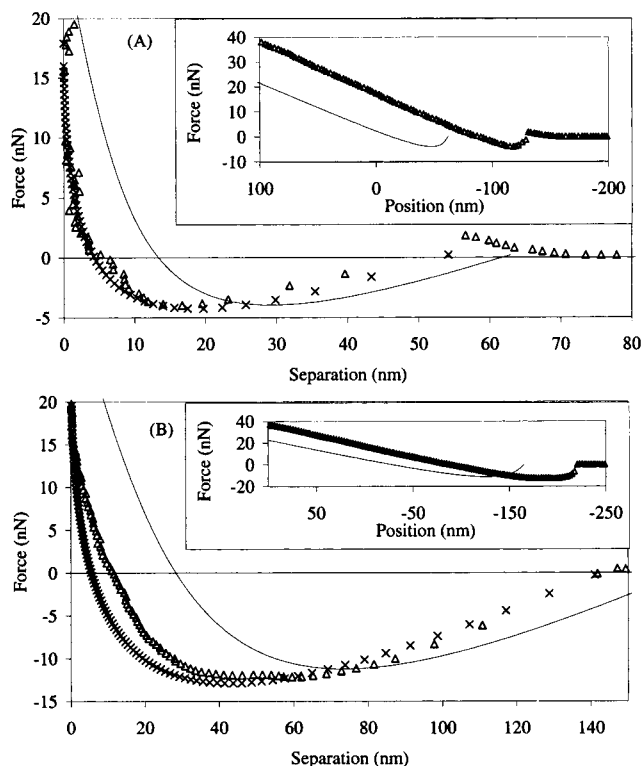


Figure 11. Measured force between hydrophobic surfaces in water compared to that calculated for a spreading bridging bubble. The insets show the force as a function of the drive position (arbitrary zero), including the constant compliance region that is used to calibrate the measurement of the cantilever deflection and to set the zero of separation. The experimental data (triangles) are taken from ref 16. The calculations are as for the canonical case in Figure 10A, except that in (A) the bubble size is $R_b = 75$ nm ($z_b = 62$ nm) and the initial radius is $r_{s0} = 40$ nm, and in (B) the bubble size is $R_b = 200$ nm ($z_b = 165$ nm) and the initial radius is $r_{s0} = 115$ nm. For the calculations, the curve is the actual force versus actual separation, whereas the crosses are the apparent force and apparent separation, as obtained by doing a calibration at an applied load of 20 nN, as in the experiments.

reversed at the maximum load and the surfaces are pulled apart (separation). The linear or constant compliance regions are used to calibrate the force sensor and to set the zero of separation. The different slopes of the two curves evident in the figure is due to the fact that the surfaces were not in intimate contact at the maximum applied load. This observation provides a way to avoid artifacts that arise in the analysis of experimental data from using the wrong zero and calibration factor. Generally speaking, the correct values may be obtained prior to the largest applied load.

The present theory is compared to experiment in Figure 11. The measurements were performed for a colloid sphere (diameter $20.6 \mu\text{m}$) interacting with a planar surface;¹⁶ to the extent that the Derjaguin approximation accounts for size and geometry (but see Figure 5), they should be comparable to the present sphere–sphere results with $R = 20 \mu\text{m}$. The bulk contact angle of the surfaces used in the measurements was estimated to be $\theta_{\text{slv}} \geq 100^\circ$.¹⁶ The drive velocity, sampling frequency, and spring constant used in the experiments are all as in the canonical case of Figure 10A.

Qualitatively, features of the experimental data strongly resemble those mentioned in the discussion of Figure 10. These include the initial fast jump toward contact (large spacing between successive points), the slowing down of the cantilever while the attraction continues to increase,

a relatively flat force extremum, and a relatively soft compliance region approaching apparent contact. In view of the qualitative similarity with the above calculations, it is clear that suitable choices of bubble size and drag coefficient will be able to account quantitatively for the data. Preattachment forces have not been included in the theory, and so the steep repulsion prior to the jump toward contact (most evident in the experimental data in Figure 11A), is not accounted for here. It may be seen that in both parts of the figure the surfaces initially move faster in the experiment than in the theory, which reflects the limitations of the theory immediately after attachment, as discussed above. Apart from the preattachment repulsion and the initial acceleration, the present theory gives a good account of the experimental data. The depth of the force minimum, its width, and the shape of the soft precontact region are quantitatively described by bubbles of size $R_b = 75$ nm, (Figure 11A) and $R_b = 200$ nm (Figure 11B), and a drag coefficient of $b = 20 \text{ kN s m}^{-2}$. Over the exhibited ranges of (A) and (B), the average velocity of the contact radius is $\dot{r}_s = 9.7$ and $10.2 \mu\text{m s}^{-1}$, respectively.

In the case of the theory, both the actual and the apparent forces are shown. The latter is obtained by mimicking the analysis of an AFM measurement. As shown in the inset, the so-called constant compliance region, which is the region where the measured deflection signal varies linearly with driving position, is used both to establish the zero of separation and to calibrate the deflection signal. As shown in Figure 10, for large bubbles the surfaces may not come into intimate contact unless very large loads are applied, by which time the deflection signal may well have saturated. In the case of Figure 11 the calibration was performed at a load of 20 nN in both the theory and experiment. With experimental scatter it is often difficult to be certain whether the constant compliance region really is linear, and there is no real way of ensuring that the surfaces have reached intimate contact. (But see the discussion of the inset of Figure 10B.) The shift and rotation of the theoretical curves in Figure 11 are typical of what may happen when the surfaces have not reached final contact. In other words, the force and separation measured in an experiment are the apparent ones, and these do not give the actual force law unless the measurement has been calibrated with the surfaces in actual contact.

Conclusion

The problem of shape optimization by free energy minimization is a general one, and the present algorithm of finding the coefficients of a polynomial expansion by moving in the direction of the conjugate forces is robust, efficient, and generally applicable. The accuracy and computational complexity are readily controlled by the order of the expansion, and as a variational procedure it is superior to the traditional methods of solving the Euler–Lagrange differential equation. The technique lends itself to the imposition of constraints and readily enables the evaluation of thermodynamic forces under a variety of conditions. Here a novel generalization to the dynamic situation was pursued, and again it was found that the algorithm was both tractable and stable.

Specific results were obtained here for a bubble bridging two colloidal spheres in water. It was found that for hydrophobic surfaces the bubbles were concave in shape and that there were two free energy minima, corresponding to submicroscopic bubbles, which are stable at separations beyond about 100 nm, and microscopic bubbles, which are stable when the surfaces are within

about 50 nm. Over a range of intermediate separations there is an energy barrier between the two branches, which makes the bubbles on approach and on separation hysteretic. For hydrophilic surfaces (i.e., those with a contact angle less than 90°), the bubbles are convex and there is a single energy minimum, which occurs at submicroscopic radii.

The force between the colloid spheres due to the bridging bubble is in general monotonically attractive. It is much stronger on the microscopic branch than on the submicroscopic branch, and it is discontinuous at the spinodal transition between them. The magnitude of the force on the microscopic branch scales to leading order with the radius of the colloidal spheres, as predicted by the Derjaguin approximation, but there are nonnegligible higher order corrections to this. On the submicroscopic branch the attraction is independent of the sphere size. The size of the bridging bubble depends on the amount of gas entrapped (which determines the bubble size prior to bridging), and the attraction is larger for larger sized bubbles. The attraction also increases with surface hydrophobicity. For hydrophilic surfaces, and for bubbles with the contact radius pinned, the force is attractive and almost constant at large separations, and it becomes softly repulsive at small separations.

An analytic result was derived that approximated the bubble as a cylinder with radius determined by free energy minimization. The expression is restricted to the microscopic branch where it accurately gave the size of the bubble and the attraction between the spheres, and also the spinodal separation for microscopic bubbles. For the case of capillary adhesion, comparison of this cylindrical approximation with a classic approximation that utilizes the Laplace pressure and a certain spheroid of revolution for the complement of the bubble shape showed that the present approximation was the more accurate of the two for colloidal spheres. This new analytic approximation is applicable not only to bridging bubbles but also to bridging droplets, capillary condensation, separation-induced spinodal decomposition, and the like.

Beyond static equilibrium, the expanding bridging bubble was analyzed at the level of steady-state dynamics

by invoking a drag force on the contact radius in proportion to the contact area velocity. The drag coefficient interpolates between the free and pinned static equilibrium bubbles. It was found that the drag gave rise to a nonmonotonic force law, with a shallow force minimum, which was attractive, and a soft repulsion at small separations. Depending upon the parameters, the repulsion could prevent the surfaces coming into intimate contact for a finite applied load. In this event the apparent separation and compliance factor obtained in an experiment may differ significantly from the actual quantities, as has been previously pointed out in other dynamic contexts.^{34,35} The magnitude of the attractive minimum is decreased by increasing the drag, decreasing the size of the bubble, decreasing the initial contact radius, or driving the surfaces together faster. The velocity of the contact radius decreased over time and with decreasing separation (i.e., as the bubble expanded).

Comparison was made with the force directly measured between hydrophobic surfaces in water. All of the features present in the dynamic calculations also occurred in the experimental data. These were the long-range attraction, the initial rapid jump toward contact, the slowing of the motion even while the magnitude of the attraction continued to increase, the broad force minimum, the decreasing attraction or hook at small separations, and the soft repulsion prior to contact. An extremely good quantitative fit to the data was made with bubble sizes 75 and 200 nm and a drag coefficient of 20 kN s m^{-2} , giving an average velocity of the contact radius of the order of $10 \mu\text{m s}^{-1}$. Such good agreement supports the interpretation given in ref 16, that the measured forces are due to a submicroscopic bridging bubble and that the soft contact region was due to the dynamic expansion of the bubble. More generally they add weight to the conclusion that in some, if not all, cases the long-range attraction measured between hydrophobic surfaces is due to submicroscopic bridging bubbles.^{6,7,16}

LA991258+